Prediction and Experimental Validation of Part Thermal History in Fused Filament Fabrication Additive Manufacturing Process

Mriganka Roy[1], Reza Yavari[4], Chi Zhou[3], Olga Wodo[1,2], and Prahalada Rao[4*]

[1]Mechanical and Aerospace Engineering, University at Buffalo
[2]Materials Design and Innovation, University at Buffalo
[3]Industrial and System Engineering, University at Buffalo
[4] Mechanical and Materials Engineering, University of Nebraska-Lincoln

Abstract

Part design and process parameters directly influence the spatiotemporal distribution of temperature and associated heat transfer in parts made using additive manufacturing (AM) processes. The temporal evolution of temperature in AM parts is termed herein as *thermal profile* or *thermal history*. The thermal profile of the part, in turn, governs the formation of defects, such as porosity and shape distortion. Accordingly, the goal of this work is to understand the effect of the process parameters and the geometry on the thermal profile in AM parts. As a step towards this goal, the objectives of this work are two-fold: (1) to develop and apply a finite element-based framework that captures the transient thermal phenomena in the fused filament fabrication (FFF) additive manufacturing of acrylonitrile butadiene styrene (ABS) parts, and (2) validate the model-derived thermal profiles with experimental in-process measurements of the temperature trends obtained under different feed rate settings (viz., the translation velocity, also called scan speed or deposition speed, of the extruder on the FFF machine). In the specific context of FFF, this foray is the critical first-step towards understanding how and why the thermal profile directly affects the degree of bonding between adjacent roads (linear track of deposited material), which in turn determines the strength of the part, as well as, propensity to form defects, such as delamination. From the experimental validation perspective, we instrumented a Hyrel Hydra FFF machine with three non-contact infrared temperature sensors (thermocouples) located near the nozzle (extruder) of the machine. These sensors measure the surface temperature of a road as it is deposited. Test parts are printed under three different settings of feed rate, and subsequently, the temperature profiles acquired from the infrared thermocouples are juxtaposed against the model-derived temperature profiles. Comparison of the experimental and model-derived thermal profiles confirms a high-degree of correlation therein, with maximum absolute error less than 10%. This work thus presents one of the first efforts in validation of thermal profiles in FFF via in-process sensing. In our future work, we will focus on predicting defects, such as delamination and inter-road porosity based on the thermal profile.

Keywords: Fused Filament Fabrication, Thermal History, Finite Element Modeling, Infrared Thermocouples.

[*] Corresponding author. Email: rao@unl.edu

1 Introduction

The overarching goal of this work is to understand the effect of the process parameters and part geometry (design) on the spatiotemporal distribution of temperature and associated heat transfer rates in parts as they are being made using in additive manufacturing (AM) processes. The temporal evolution of temperature in AM parts is termed as the *thermal profile* or *thermal history*. The fundamental knowledge of the causal factors that govern the thermal history of the part is the prerequisite for three important quality-related aspects of AM [1, 2]:

- Predicting build defects, such as distortion and layer delamination, given a part geometry and particular set of process conditions.
- Establishing optimal process parameter settings and part design rules.
- Instituting closed-loop process control.

Currently, the first two of the above three aspects in AM are realized largely through empirical studies, which are time consuming and prohibitively expensive; whilst process control in AM has thus far been relegated to data-driven approaches, as opposed to strategies that encapsulate the physics of the process within a model. As a step towards understanding the thermal profile of AM parts, the objectives of this work are two-fold:

(1) Develop and apply a finite element-based framework that captures the transient thermal phenomena in a specific type of AM process called fused filament fabrication (FFF), (schematically exemplified in Figure 1).

(2) Validate the model-derived thermal profile with experimental in-process measurements of the temperature trends obtained under different processing conditions.

The FFF process, which is classified under extrusion-based AM processes, is schematically shown in Figure 1 [3, 4]. FFF is the most popular and widely used AM process, given its simplicity,

cost effectiveness, and versatility of scale and materials. In FFF, typically, a thermoplastic material in the form of a filament is heated past its glass transition temperature inside a nozzle (extruder or liquifier). This semi-molten thermoplastic polymer is extruded through the nozzle and deposited as individual tracks (roads) onto a build table (bed). The part is built layer-upon-layer by translating the nozzle relative to the build table. On cooling, the extruded thermoplastic material (extrudate) bonds to the surrounding thermoplastic material deposited in previous passes [5].

Thermoplastic materials, such as acrylonitrile butadiene styrene (ABS) and polylactic acid (PLA) are popular materials for FFF, however, a wide-range of materials including carbon-fiber reinforced polymers, and non-polymer material, e.g., concrete and regolith can be processed using the extrusion-based method for material deposition [6, 7]. The specific material considered in this work is ABS, whilst, the process condition varied is the feed rate setting, viz., the translation velocity of the extruder on the FFF machine, also called scan speed or deposition speed.

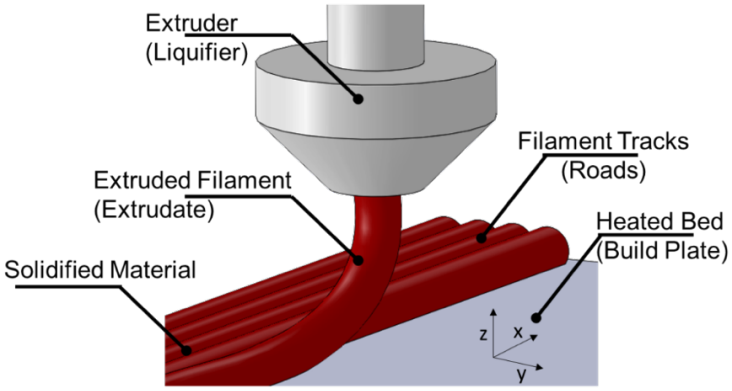

Figure 1. A schematic of the Fused Filament Fabrication (FFF) AM process.

The salient aspects of this work, in the specific context of modeling and subsequent experimental validation of FFF process, are summarized hereunder:

- The deposition process is discretized in terms of finite elements at the level of individual tracks of deposited material (road-level). In other words, the model can be termed as quasi-continuous.

- To ensure accuracy, the model closely mimics the deposition process, in that, the movement of the nozzle in the x-y-z direction (called scan pattern or hatch pattern) is replicated in the model based on examination of the machine-level G-code. We note that the speed (feed rate) and path of the nozzle (scan pattern or hatch pattern) apart from the material-related aspects influence the cooling rate, and hence the thermal profile [1].
- From an experimental vista, the thermal aspects of the process are monitored at the road-level using an array of in-process infrared non-contact thermocouple sensors. These sensors capture the thermal gradients on the top layer both ahead and behind the deposited material almost instantaneously.

The rest of this paper is organized as follows. We briefly summarize the prior works in thermal modeling and in-process measurement of thermal profile in FFF in Sec. 2. The computational model devised to understand the thermal profiles in FFF is described in Sec. 3. The experimental setup, including infrared thermal sensors and optical cameras instrumented on a FFF machine, and the in-process data therefrom used to validate the model results are reported in Sec. 4. Finally, the conclusions from this work are summarized in Sec. 5.

2 Literature Review

The literature review is divided into two parts. The first part summarizes the existing work in the area of theoretical modeling of the FFF process, whilst the second part is dedicated to the literature in the sensor-based monitoring in FFF.

2.1 Prior works in modeling of thermal behavior in FFF process.

Researchers have modeled various material-process interactions in the FFF process, namely, material behavior in the extruder [8], interactions between roads after their deposition [9], as well as mechanical [10], and thermal [11] aspects at various phenomenological scales [2]. The different

phenomenological scales in FFF are classified as: (a) the bonding behavior of the deposited thermoplastic polymer, called polymer reptation [5], (b) physical deformation of the polymer during deposition, and (c) part-level aspects, such as warping due to residual stresses [12]. We herewith summarize the pioneering works in the area of thermal modeling in FFF.

Yardimci and Güçeri [9] where amongst the forerunners to have formulated an analytical framework to model the thermal behavior of the FFF process. The main objective for their work was to provide a fundamental understanding of the inter-road behavior of the material by performing the simulations for a single layer consisting of ten roads. For this purpose, they considered the thermal interactions between the deposited roads, and accounted for their subsequent cooling and consolidation. Notably, they defined a bonding metric (i.e. bonding potential) to establish a qualitative measurement of the consolidation between roads. Their investigation, notwithstanding the elementary nature of the geometry studied and reveals that the bonding degree can vary within a single layer. In another of their related works Yardimci *et al.* [8], through analytical modeling investigated the impact of the nozzle design on the output pressure, and subsequently established the mathematical formulations to assess the location of the meltpool (molten material in near the extruder) and the degree of cooling at the extruder tip. The focus was to establish the relationship between the meltpool and the feed speed, filament size, and material diffusivity. Through their investigation, a guideline to design the extruder tip, internal duct, and liquefier length depending on their effect on extrusion was established. This model is an example of an initial modeling effort to understand the effect of the extruder characteristics in FFF.

Another scope of the thermal interactions between the deposited roads in FFF was explored by Li [13]. They assumed the roads to be of semi-infinite length (as compared to the cross-section), which allowed them to study the impact of the local heat input on the entire printed part.

Specifically, they used lumped capacitance analysis that assumes no spatial temperature variation in the zone of interest. They focused on the thermal behavior of a single road of length 50 mm and its influence on the entire part for different process parameters (extrusion temperature, envelope temperature, extruder tip size, road dimensions, fiber gap, and deposition pattern.). Through this investigation, they concluded that extrusion temperature and ambient temperature were the most influential parameters that control the thermal profile.

A different tack to modeling in FFF was introduced by Rodríguez [14], who developed a finite element model to analyze the transient heat transfer in the printed parts. However, the part was relatively simple and consisted of only five vertically stacked roads. The next milestone was achieved by accounting for the behavior of the melt pool by Zhang and Chou [11]. They developed a three-dimensional thermal model of the melt-pool in FFF for a simple cuboid geometry with 4 layers consisting of 40 roads each. This model was later used by Zhang [12] to investigate the residual stress in FFF process. They related three parameters, namely, print speed, layer thickness and, road width, with the part distortion during a printing process demonstrating that scan speed is the most significant factor affecting the distortion. This numerical experiment was conducted on a specimen of size 40×10×1.016 mm (8 layers with 40 roads each).

Substantial progress on the modeling front has been made by Costa *et. al*. [15], who studied the thermal conditions in FFF using ABAQUS® with particular emphasis on examining the effect of convection and radiation (with the environment, entrapped air), and conduction (between the filaments and between the printed part and support) on the heat transfer phenomenon. They made important observations for subsequent models, including our model presented in this paper. They concluded that convection and conduction have the highest impact on the thermal profiles. Conversely, the convection and radiation in the air pockets between ellipsoidal filaments have a

negligible effect. This observation reaffirmed justification for the assumption of the deposited road having a rectangular cross-section.

In summary, several models to study the thermal behavior of layer-by-layer deposition in FFF are available. However, none of these was used to study the thermal behavior of realistic parts. Specifically, previous efforts focused on understanding the physical phenomenon of AM through modeling but experimental validation of computational models through in-process sensor data remains to be investigated. This extant gap is addressed in this paper.

2.2 Prior works in in-process monitoring in FFF.

In one of the earliest works in sensor-based monitoring in FFF, Bukkapatnam *et al.* [16] investigated vibration in FFF, comparing mechanistic lumped-mass models with experimentally obtained vibration sensor data, and demonstrated the ability to distinguish process abnormalities. Fang *et al.* [17] used machine vision techniques to detect defects in FFF of ceramics based on optical imaging of each layer during the build. Cheng and Jafari [18] examined the build surface using image intensity information and classified defects into two types, namely, randomly occurring defects, and anomalies due to assignable causes, e.g., improper extruder tool path. He *et al.* [19] studied on one of the common extruder nozzle clog problem in the FFF process with the help of the IR camera. They extracted features from IR camera images of each layer and analyzed to discern the nozzle from normal to clogged condition. Wu *et al*. [20] applied the in-process acoustic emission sensing to collect the elastic waveform signals which is released by the printed material. They concluded that the acoustic emission signals detect the common machine failure such as material run-out and filament breakage. However, the wide frequency range and high sampling rates of acoustic emission sensing process requires high sampling frequency data acquisition, and moreover, is not related directed to the thermal aspects.

Dinwiddie *et al.* [21] acquired the temperature profile of the part during the printing process with two different thermal cameras. One was located outside of the chamber, behind a window. The other thermal camera was located inside the chamber and collected the reflection of the extruder tip from a gold mirror. Despite the expensive costs of two thermal cameras, another factor in FFF that hampers thermo-optical measurements in FFF is the small distance between the extruder tip and substrate. Kousiatza and Karalekas used the strain sensors and thermocouples as their real time monitoring sensors at different layers of the printed part [22]. They reported that the magnitude of the induced residual strains has a direct correlation with the temperature field in the FFF process. Herefore, monitoring the temperature profile of the process can be informative for quality assurance purposes. However, the fluctuations of the temperature are not prominently evident in the thermocouple sensors since top surface being deposited is at a much further location from the thermocouples as done. Thus, an infrared sensor, which is mounted to the extruder at a constant distance from the extruder tip during the printing, as implemented in this work is consequential and more informative to track the temperature profile at the top surface.

3 Transient Thermal Modeling of the FFF process

The degree of bonding of adjacent tracks deposited during the FFF process determines the functional integrity of the part, such as its strength, and is primarily governed by thermal aspects of polymer diffusion slightly above the glass transition region. In this regime, intermolecular forces in the polymer matrix are weak and adjacent extrudates (deposited material) form bonds through diffusion. When the temperature at the interface of two surfaces is higher than the glass temperature the polymer-chains transition across surrounding surfaces through a process termed as *reptation* [23]. The strength of the bond is dependent on the average length of the polymers that penetrate through the interface, called minor chain length. The minor chain length, in turn, is a

function of the temperature profile (heat flux) at the consolidating surface, and lastly, the heat flux governs the bonding degree. Following this reasoning, the part defects, e.g., delamination and warping, are a direct result of the poor bonding between adjacent extrudates, which in turn is contingent on the bonding temperature. Accordingly, predicting the thermal behavior of the deposited roads and quantifying its dependence on process parameters is consequential for determining the functional integrity of FFF parts.

3.1 Mathematical formulation of the model

In this section, we introduce the mathematical model that describes the thermal phenomena in FFF. To keep the development brief, the following assumptions are imposed:

- The nozzle is treated as a moving heat source, with the heat influx originating from the extruded material deposited at high temperature.
- The material extruded is considered to be homogeneous and isotropic. The pores in the filament and possible change in density due to material vaporization is neglected.
- The material characteristics are assumed to be static, in that the specific heat capacity, density, and conductivity are considered to be temperature independent.
- The latent heat generation due to the material changing from liquid to solid are not considered.
- The shape of the filament deposited is assumed to remain identical. In other words, the shrinkage in the material due to cooling is neglected. Likewise, the effect of warping and distortion on the shape of the deposited roads is neglected.
- The ambient temperature (T_{am}) and base temperature T_b are also considered constant during the process.

The main thermal heat transfer phenomena in FFF as per the different interaction zones are depicted in Figure 2, these are further delineated hereunder.

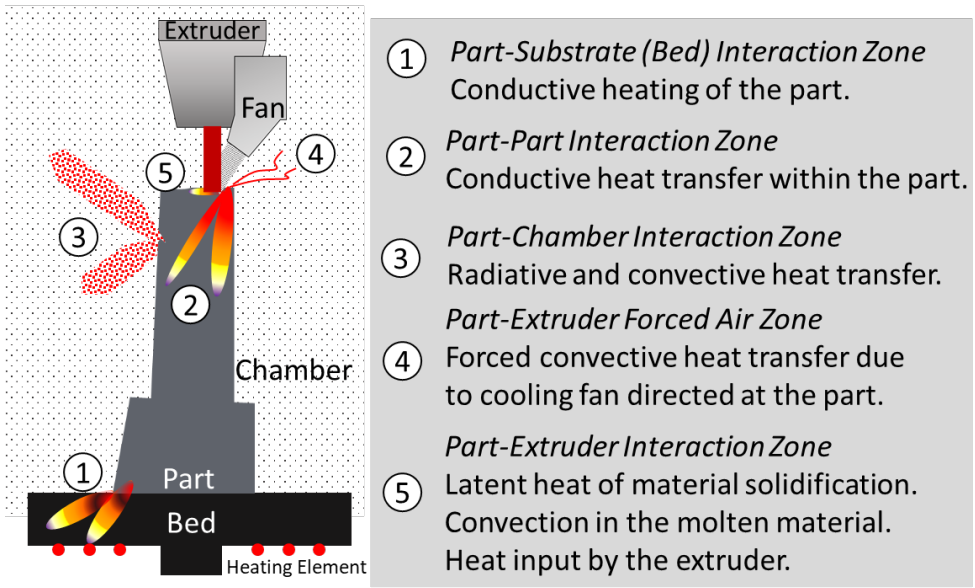

Figure 2: The salient heat transfer phenomena in FFF process stratified per the five interaction zones.

(1) *Part-Substrate (Bed) Interaction Zone*: The part is deposited on a substrate (in this work painters' tape) which is heated through a heater integrated inside the bed. The heating of the substrate prevents uneven cooling of the part and hence avoids thermal stress-related warping. The heat transfer mechanism in this zone of the part corresponds to heat conduction with additional heat source supplied through table. In this work, the bed is maintained at 85 °C (358.15 K). We note that there is a control mechanism in the resistance heater provided in the aluminum heat bed on the Hyrel Hydra that is activated when the set temperature is outside a threshold (roughly 2 °C).

(2) *Part-Part Interaction Zone*: As new semi-molten material is added it contacts the previously deposited tracks (roads). Heat is transferred between roads and layers within the part through conductive heat transfer under the assumption of perfect contact between individual adjacent roads.

(3) *Part-Chamber Interaction Zone:* The heat is dissipated from free surfaces of the part into the chamber due to radiation and convection. In some FFF systems the chamber is heated. In this

work, the chamber was not heated, but was enclosed and maintained at an ambient temperature of 30 °C (303.15 K).

(4) *Part-Extruder Interaction Zone:* Cool air is often blown over the freshly deposited semi-molten material from a fan integral to the extruder to aid quick solidification. This feature is valuable while building long unsupported spans (overhang features). Thus, forced convective transfer takes place between the part and chamber due to air blowing over the part. This fan was not active for the experiments used in this work. Furthermore, there is another fan directed at the extruder (not the part) to avoid overheating of the extruder. This fan is assumed not to influence the process.

(5) *Part-Extruder Interaction Zone*: At the point where the material is deposited, three heat transfer processes are active, these are: heating of the part due to the extruder (treated as a moving heat source transferred through deposited material at a higher temperature), latent heat generation due to material solidification, and the convection within the molten material before it solidifies. In this work we ignore the latent heat and convection effects within the meltpool.

The factors that affect these phenomena comprise material properties, ambient temperature, deposition speed, part geometry and associated layer thickness, as well as deposition pattern. The model used in this paper accounts for these factors and thermal phenomena. The thermal behavior within the deposited material is mathematically represented by the transient heat equation:

$$\rho c_p \frac{\partial T}{\partial t} = \nabla(\lambda \nabla T) + \dot{q} \quad in\ \Omega(t) \tag{1}$$

where, T is the temperature, ρ is the density of the deposited material (kg/m^3), c_p is the specific heat capacity (J/kg·K), λ is the thermal conductivity (W/m·K) and q represents the external heat source per unit volume (J/m^3). The computation domain $\Omega(t)$ evolves with deposition and hence

is a function of time. In other words, the part geometry changes as the material is deposited, this is accounted for through the element birth-and-death simulation process.

$$\Omega(t) = f_{\Omega}(t) \tag{2}$$

The interaction of the printed material with the environment is considered as a boundary condition. The heat is dissipated through free surfaces of the printed part to the environment (by convection and radiation). This effect is modeled as a boundary condition applied on all free outer surfaces of the printed part given by the following equation:

$$q_{surf} = h(T - T_{am}) + \kappa(T^4 - T_{\infty}) \quad on\ \Gamma_f(t) \tag{3}$$

where, h is the heat convection coefficient (W/m^2·K) of the material at the ambient temperature, κ is the emissivity of air. Temperature T_{am} is the printing chamber temperature (K) during the print, T_{∞} is the reference temperature (K) at an infinite distance for radiation. The ambient temperature is assumed to be minutely affected by the deposition and hence, $T_{am} = T_{\infty}$.

However, as explained before, the free surfaces ($\Gamma_f(t)$) evolves with time as more material is added to the printed part. When new roads are added, new surfaces are exposed to the cooling, consequently the free surfaces need to be updated in the model. At the same time, some of the surfaces are covered with newly added material and are no longer subjected to these boundary conditions, and they need to be removed from the model.

Typically, in most FFF machines, the bed is heated to avoid uneven cooling of the part, which is modeled by imposing constant temperature T_b through following boundary condition:

$$T_{\Gamma}(t) = T_b \quad on\ \Gamma_b(t) \tag{4}$$

Similar to the previous boundary condition, the base surface changes with deposition time. However, in this case, the surface needs to be updated until the first layer is completely deposited, which is encapsulated as:

$$\Gamma_b(t) = \begin{cases} f_\Gamma\,(t) & \forall\, 0 \leq t \leq t_{layer} \\ f_\Gamma(t_{base}) & \forall t > t_{layer} \end{cases} \tag{5}$$

where, t_{base} is the time required for the first layer to be printed.

As material is being added to the printed part, computational domain increases contingent on the speed and path of the extruder. The temperature of the locally added volume is set to the deposition temperature T_d:

$$T(t_d) = T_d \quad in\, \Omega(t) \tag{6}$$

In summary the mathematical model simply consists of the governing equation Eqn. (1), two boundary conditions Eqn. (3) and Eqn. (4), and a local initial condition Eq. (6). However, constructing the computational model and solving it requires surmounting the following two major challenges:

1) *Continuous deposition process*: Due to continuous deposition in FFF the computational domain increases with deposition. The exact progression of the domain depends on the part geometry, layer thickness and deposition pattern.
2) *Time dependent cooling surfaces*: The printing process also requires that continuous changes are made to surfaces subjected to boundary conditions. This again depends on several process material factors, including geometry.

Evidently, the foregoing challenges are geometry dependent and coupled with the deposition pattern. In practice, this implies that the time varying computational domain and all the surfaces

for initial and boundary conditions need to be determined for a specific part. As the complexity of the part increases, the tracking of the surfaces becomes more geometrically challenging.

3.2 Computational model of the heat transfer in the FFF process.

In this paper, the governing Eqn. (1) together with boundary and initial conditions are solved using the Abaqus® commercial finite element method (FEM) software [24-27]. The part geometry is discretized using custom code developed in house. The deposition is discretized in time as unit depositions. The elements are numbered such that it is evocative of the deposition path encoded in the G-Code of the machine which dictates the path taken by the extruder, and as a consequence, gradual activation of the local deposition is simplified.

The discrete deposition approach was implemented through activation of set of elements that constitute one deposition unit. As the deposition proceeds, new elements are activated in the computational mesh. The temperature of the activated nodes is initialized with the temperature matching the deposition temperature (T_d). Further, the side and top surfaces of deposited unit exposed to the environment are subjected to external convection and radiation fluxes according to Eqn. (3). The location of the corresponding free surfaces is tracked in the user-defined Abaqus-specific subroutine called DFLUX. We note that even for a simple geometry and scan pattern, tracking the free surface is fraught with complexity. For example, for a cuboid-shaped geometry, at any given time (t) the direction of the extruder is given by:

$$d = (-1)^{\left\lfloor \frac{t}{t_{road}} \right\rfloor} \tag{7}$$

where, d represents the direction of the print and t_{road} is the time required to deposit a single road ($t_{road} = \frac{road\ length}{print\ speed\ (v)}$). We use the direction d to first determine the position of the extruder during the deposition, next to guide the free surface tracking and finally to apply the boundary

conditions. Formally, for the simple cuboid geometry of the part, the extruder position (x_e, y_e, z_e), given in units of length (m), can be expressed as:

$$\begin{aligned} z_e &= \lceil t/t_{layer} \rceil \cdot h_d \\ x_e &= \lceil (t - (H-1) \cdot t_{layer})/t_{road} \rceil \cdot w_d \\ y_e &= \begin{cases} (t - \lfloor t/t_{road} \rfloor) \cdot v_d & \forall\ d = 1 \\ B - (t - \lfloor t/t_{road} \rfloor) \cdot v_d & \forall\ d = -1 \end{cases} \end{aligned} \tag{8}$$

Once the position of the extruder is determined, the free surfaces and according boundary conditions can be applied for nodes with following coordinates (x, y, z):

$$\begin{aligned} x = 0 \ or\ y = 0 \\ x = L\ or\ y = B \\ x < x_e\ and\ z = z_e \\ d \cdot y < d \cdot y_e\ and\ z = z_e\ and\ x < x_e + l_d \end{aligned} \tag{9}$$

where L is the length of the part for x direction and B is the breadth for y direction as shown in Figure 3. The unit depositions are of size (l_d, b_d, h_d), given in units of length (m). When a new set of elements is added to the mesh, the boundary conditions needs to be updated accordingly. Specifically, for surfaces buried under just added set of elements the boundary conditions needs to be removed, while for the free surfaces just exposed to the environment the boundary conditions must be added to the model.

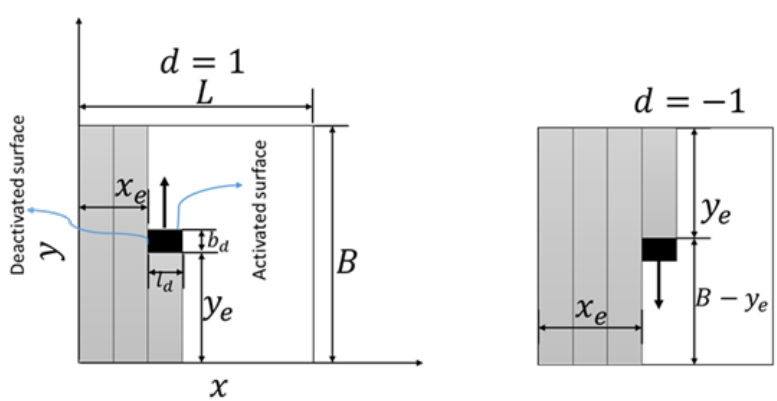

Figure 3: Discretized deposition pattern implemented in this work. Two deposition directions are considered (left panel: positive direction, right panel: negative direction). The figure depicts the auxiliary quantities used to determine the local position of the extruder and the coordinates required to update boundary conditions and initiate the temperature of just added or activated elements.

The deposited roads have a cross-section of ≈ 0.2 mm^2 that are discretized into four elements. With such fine discretization, the mesh for a print of a 25 cm^3 volume consists of approximately 1 million nodes. The mesh was generated to capture the thermal behavior without requiring considerably high computational effort, with size of element chosen through convergence analysis. The material properties are obtained from standard data sheets for ABS thermoplastic. The ambient temperature (T_{am}) in Eqn. (3) is the environment temperature and is set to $303.15\ K$ (30°C) during the printing process. All other material properties, process parameters, and simulation details are given in Table 1.

Table 1: ABS material specific parameters, and simulation hyper parameters used in this work.

Material Properties	Conduction coefficient (λ)	0.17 W/m/K
	Density (ρ)	1050 kg/m^3
	Specific heat (c_p)	2020 J/kg/K
	Emissivity for air (κ)	0.90
	Convection coefficient (h)	21 W/m^2/K
Process parameters	Ambient temperature (T_{am})	303.15 K
	Base temperature (T_b)	358.15 K
	Print speed (v)	0.02, 0.03, 0.04 m/s
	Layer Thickness	0.0002 m
	Road Width	0.001 m
Simulation Details	Element size	0.0001 × 0.0001 × 0.0001 m^3
	Element type	8 node linear thermal brick element (DC3D8)
	Integration	Full integration
	Initial Condition	503.15 K
	Activation set size	0.0004 × 0.0001 × 0.0002 m^3

4 Experimental Validation

4.1 Sensing setup

In this study we used a Hyrel Hydra FFF machine. This machine is instrumented with multiple in-process sensors, including three infrared K-type thermocouples sensors (Exergen-150046). The infrared sensors measure the temperature, and are calibrated for a linear response up to 200°C. The temperature measurements are acquired at a sampling rate of 10 Hz, and conditioned through a

National Instruments data acquisition (NI DAQ 9188) board. Thus, the data is time stamped, and with help of visual demarcation the data (via an optical camera) it is related to the position of the nozzle. Figure 4(a) and (b) show the schematic, and Figure 4(c) and (d) depict the actual sensing array implemented in this work.

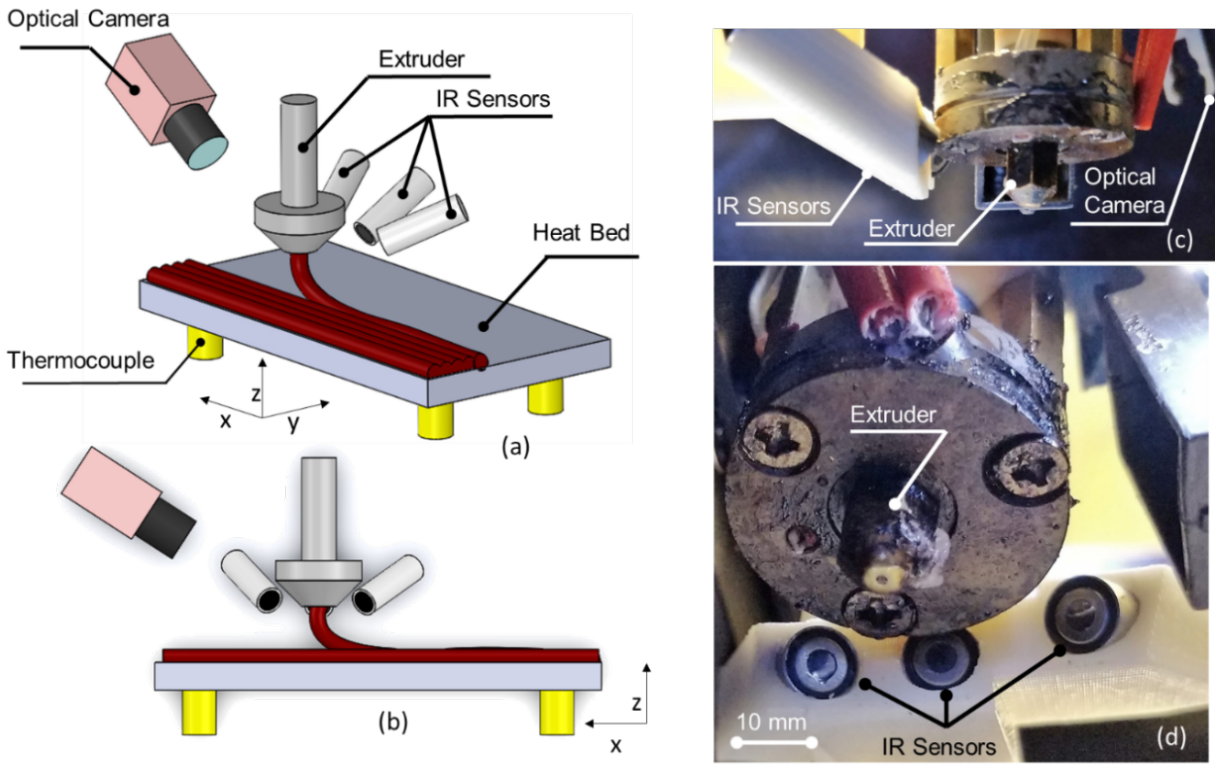

Figure 4. (a) and (b) schematic diagram of the setup, (c) and (d) photograph of the actual implementation.

Figure 5 shows the position of the middle infrared sensor, and the manner in which it records the temperature of an individual track of deposited material. As shown in Figure 5, the middle IR sensor peers at the part at an angle, and hence the area over which temperature is measured for a deposited track tends to be elliptical in shape. The measured area has the point of extrusion as the center and moves along with the extruder. Besides, the sensor also scans a portion of the extruder. To account for these eventualities, and reconcile the temperature data acquired by the sensors with the trends predicted by the thermal model, we further processed the latter.

To explain further, we averaged the temperature distribution predicted by the simulation over an elliptical area identical to the area scanned by the IR temperature sensor. This area (≈ 24 mm^2) is estimated from a solid model reproduction of the experimental setup as shown in Figure 5, the middle IR sensor overlooks the print at an angle, which makes the area measured to be elliptical in shape. The area has the point of extrusion as the center and moves with the extruder. Besides, the sensor also scans a portion of the extruder.

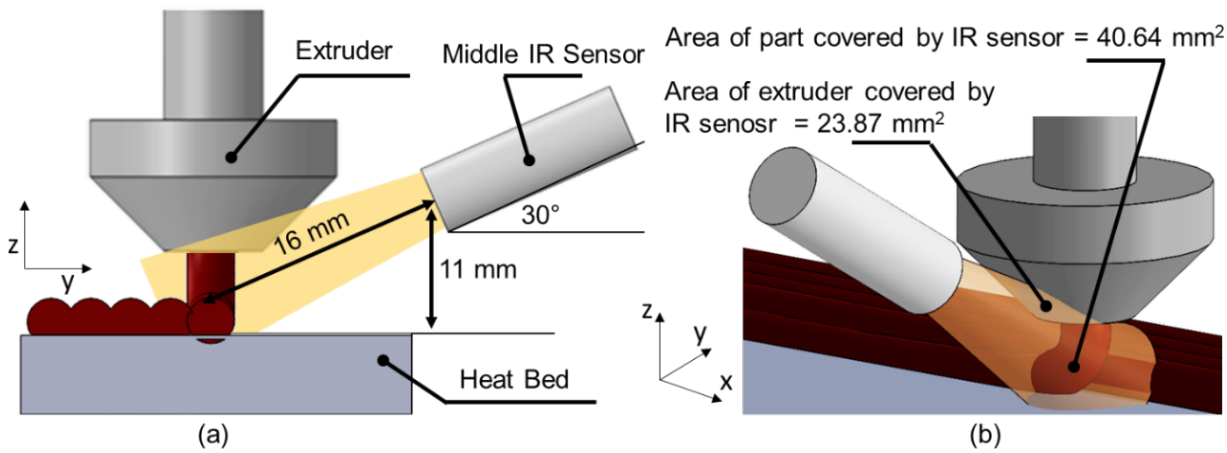

Figure 5. (a) Position of the middle infrared sensor to the extruder, (b) the covered area of the extruded material and hot extruder by the middle infrared sensor.

4.2 Test Geometry and Process Conditions Chosen for Experimental Validation

The test part shown in Figure 6 is used for empirical testing. It is essentially a two-tier stepped-pyramid type object. The test part has a total of 10 layers, each tier accounting for 5 layers; the layer height being 0.2 mm. We maintain all the processing parameters delineated in the Table 2 constant. We note that the test part used embodies a change in the surface area with progressive deposition, which in turn has a consequential effect on the thermal history. In other words, instead of the same cyclical, repeating pattern in the temperature trends, the geometry shown in Figure 6 entails a complex part design-thermal pattern interaction.

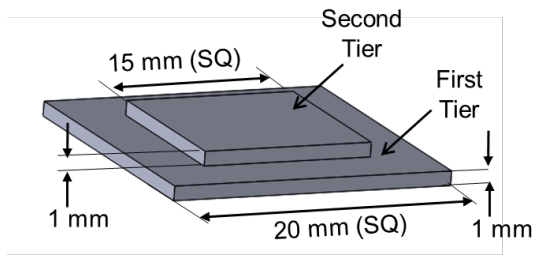

Figure 6. Geometry of the stepped pyramid-shaped test artifact studied in this work. This particular part geometry has two tiers, the second of which has a smaller surface area than the first. As a result, the thermal patterns will vary as the part is being deposited.

Table 2. Printing Parameters that are maintained constant during experimentation.

Parameter	**Value**	**Parameter**	**Value**
Deposition width	1 mm	Layer thickness	0.2 mm
Scanning speed (feed rate, (v))	20, 30, 40 mm/s	Nozzle temperature	503.15 K
Hatch pattern	Linear	Ambient temperature (T_{am})	303.15 K
Bed temperature (T_b)	358.15 K	Material flow rate	20, 30, 40 mm/s
Total number of layers	10	Infill	100%

The feed rate (v) is varied at three levels of 20, 30 and 40 mm/s. The variation of the feed rate levels leads to change in the feed rate to flow rate ratio, and is thus connected to the characteristics of the extrudate. A large feed rate to flow rate ratio results in so-called stringy deposition of the road. Whereas, a small feed rate to flow rate ratio causes inordinately thick roads to be deposited. If the height of the road exceeds the set layer thickness, the deposited material will make contact with the extruder leading to clogging of the nozzle. The effect of feed rate to flow rate ratio has a discernable effect on the quality of the part. The effect of feed rate to flow rate ratio on the surface finish and nozzle clogging phenomena is discussed by Rao *et al*. [28]. Hence, in this work the material flow rate is also adjusted so that the feed rate to flow rate ration is always unity (= 1).

An example results from simulation depicting the progression of the temperature field is shown in Figure 7. The figure shows the evolution of temperature field for three selected snapshots and three different feed rates. The left-most column depicts the temperature distribution for the third layer of the first tier. The middle column of this figure depicts the temperature distribution for the first layer of the second tier. Finally, the right-most column of Figure 7 depicts the

temperature distribution of the second layer for the second tier. These simulation results demonstrate the complexity of temperature distribution during the FFF process.

It is observed from Figure 7 that the temperature distribution for the second layer is significantly different from the first tier. On average, the temperature rises by about 10° C. Specifically, for the second tier, the increased temperature zone is more widespread. This means that the second tier of the part is kept at higher temperature for longer time. This may result in higher degree of bonding, as polymer chain have more time and energy to inter diffuse into adjacent road and layer. For example, compare the columns for the time of 40 seconds and 140 seconds.

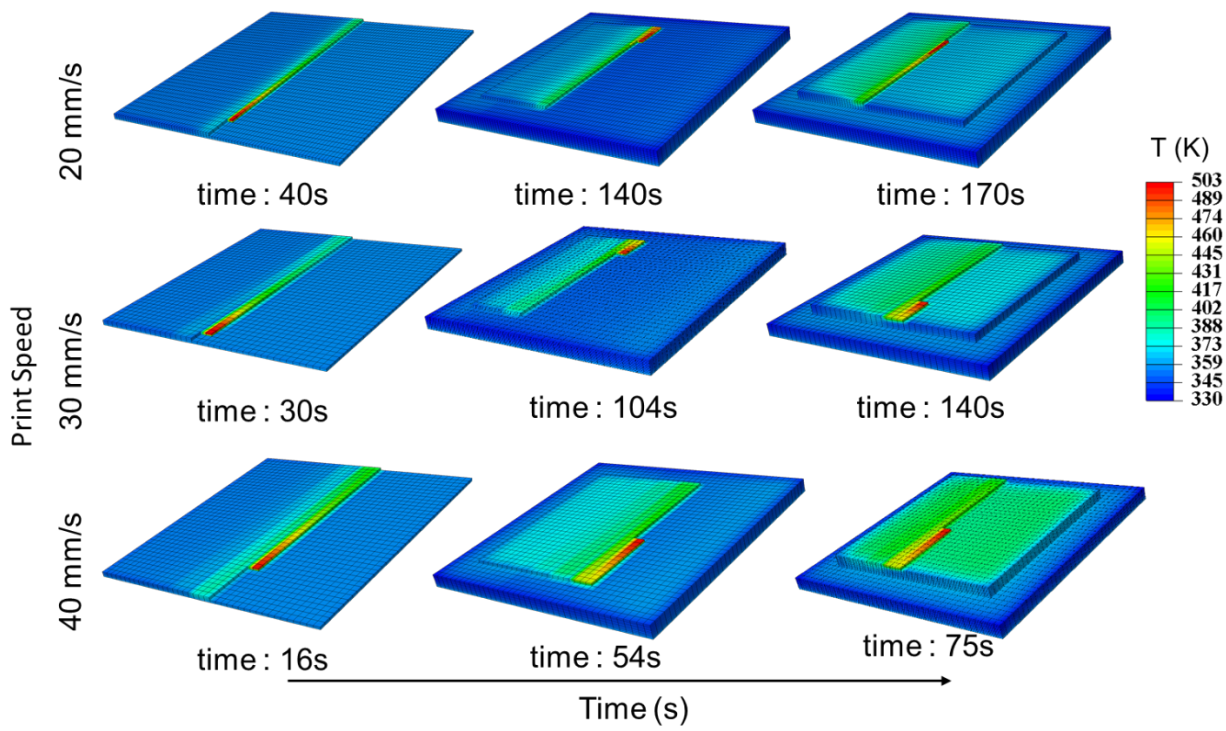

Figure 7: Temperature distribution snapshots captured during the FE-simulation of the deposition process for different feed rates. The left-most column shows the approximate middle of the third of five layers of the first tier of the test artifact. The middle column captures the first layer of the second tier (sixth layer overall), and the right-most column depicts the second layer of the second tier (seventh layer overall). These snapshots reveal the intertwined nature of the feed rate and thermal history.

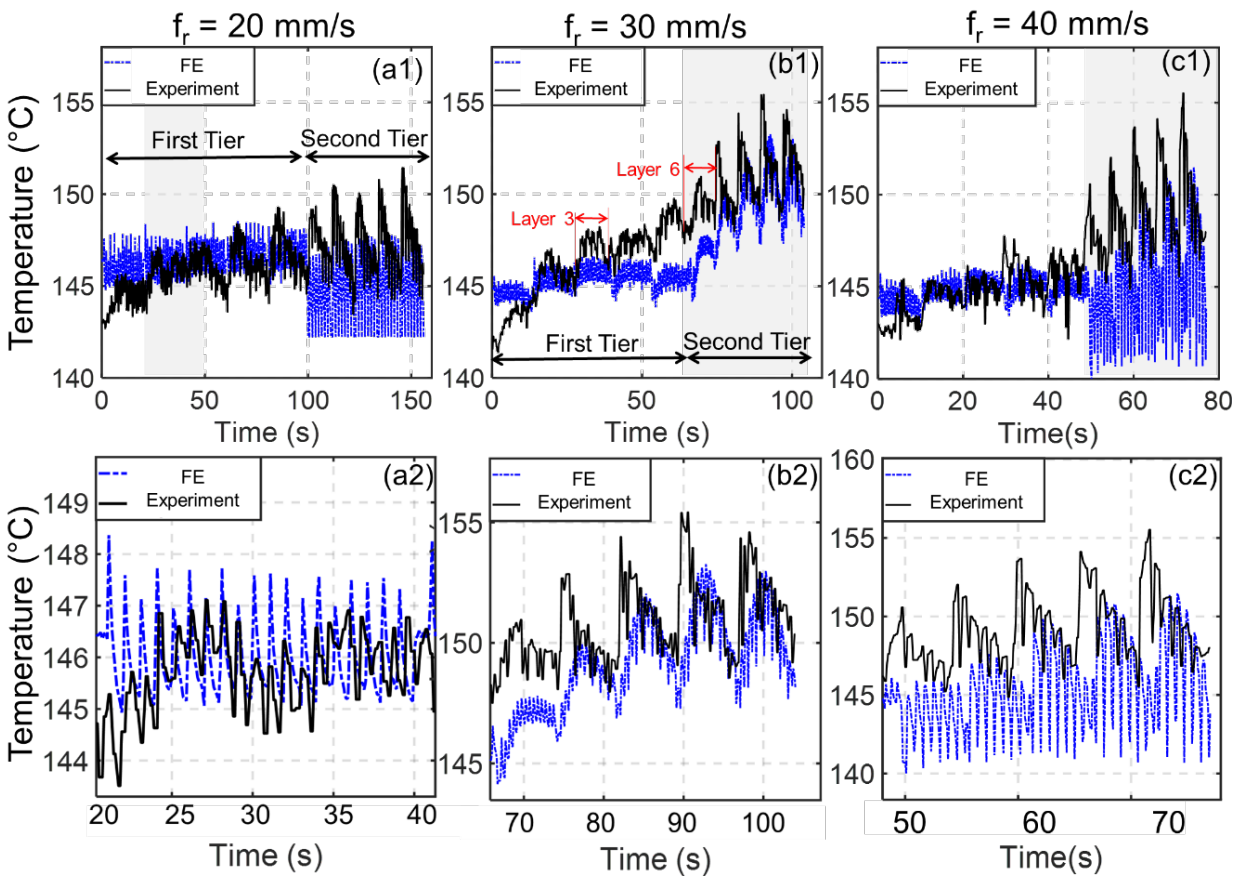

Figure 8. The experimental data (thick lines) is juxtaposed for the FE-model derived predictions (dotted line) for different feed rates (f_r).The top row (a1) through (c1) shows the overall trends; the bottom row (a2) through (c2) shows a zoomed in portion highlighted in the top row.

Next, the effect of feed rate on the thermal profile is depicted in Figure 8, which juxtaposes the measured surface temperature profiles with the model-derived predictions. The following inferences are drawn based on the trends observed in Figure 8.

- The surface temperature increases substantially for the so-called second tier of the test artifact, compared to the first layer. This is because, given the smaller area of the second tier (15 mm × 15 mm), the extrudate has shorter time to cool between deposition of individual roads.
- The start of deposition in each layer corresponds to a periodic pattern, this periodic pattern occurs because the infrared thermocouple measures the average temperature over an area. As

the layer cools, the average temperature over the rest of the area is lower than the currently deposited road.

- Within each layer another pattern is observed, which corresponds to the deposition of an individual road within each layer. We note that material is deposited in one direction only, hence, after a hatch is deposited, the extruder returns to the starting position of the next hatch, without depositing material on the way back.

From Figure 8 it is evident that the trends derived from the finite element (FE) model match the experimental data, and location of the temperature spikes; albeit the magnitude (amplitude) of the predicted pattern is within 10 °C for the worst-case scenario. Pertinently, the close agreement in experimental and model-derived temperature profiles related to temporal location and trend in the signal is replicated across the different feed rates. The maximum absolute error between the predicted temperature profile with FE-analysis with measured temperature profile in experiment for the three feed rates studied are as follows: for feed rate of 20 mm/sec, the error is 5.9%; 30 mm/sec, error 4.8%; and 40 mm/sec, error 8.6%.

5 Conclusions and Future Work

In this work we developed and applied a finite element-based transient model to explain the effect of the material feed rate on the temperature profile in the FFF process. The thermal profiles predicted by the model were experimentally validated on a Hyrel Hydra FFF machine integrated with multiple non-contact infrared thermocouple sensors. Specifically, the temperature variations resulting from a change in the layer geometry of a test object, and due to the process condition (feed rate), were predicted using the FE model within 10% of experimental observations. This work therefore explains how and why the temperature profile in FFF is linked to the process parameters and part design. This knowledge is the foundational basis for determining the optimal

part geometry and process conditions, as well as model-based closed loop control of the FFF process [29]. Our future work in the area will endeavor to answer the following questions:

1. What is the effect of different materials, and more complex part geometries on the temperature profile?
2. What is the effect of the temperature profile on the bonding degree and functional properties of the part?
3. What should be the corrective action once a defect is detected and can such a corrective action be recommended by a theoretical model.

Acknowledgements

One of the authors (PKR) thanks the NSF for funding his research through the following grants CMMI-1719388, CMMI-1739696 and CMMI-1752069 (CAREER) at University of Nebraska-Lincoln. Specifically, the concept of in-process sensing, and model-based defect detection and isolation was funded through CMMI-1752069 towards a *correct-as-you-build* smart additive manufacturing paradigm.

References

[1] Talagani, M., DorMohammadi, S., Dutton, R., Godines, C., Baid, H., Abdi, F., Kunc, V., Compton, B., Simunovic, S., and Duty, C., 2015, "Numerical simulation of big area additive manufacturing (3D printing) of a full size car," SAMPE Journal, 51(4), pp. 27-36

[2] Bikas, H., Stavropoulos, P., and Chryssolouris, G., 2016, "Additive manufacturing methods and modelling approaches: a critical review," The International Journal of Advanced Manufacturing Technology, 83(1-4), pp. 389-405

[3] Gibson, I., Rosen, D. W., and Stucker, B., 2010, Additive Manufacturing Technologies – Rapid Prototyping to Direct Digital Manufacturing, Springer, Boston, MA.

[4] ASTM, 2012, "F42 - Standard terminology for additive manufacturing technologies," ASTM International.

[5] Bellehumeur, C., Li, L., Sun, Q., and Gu, P., 2004, "Modeling of bond formation between polymer filaments in the fused deposition modeling process," Journal of Manufacturing Processes, 6(2), pp. 170-178

[6] Duty, C. E., Kunc, V., Compton, B., Post, B., Erdman, D., Smith, R., Lind, R., Lloyd, P., and Love, L., 2017, "Structure and mechanical behavior of Big Area Additive Manufacturing (BAAM) materials," Rapid Prototyping Journal, 23(1), pp. 181-189

[7] Khoshnevis, B., 2004, "Automated construction by contour crafting—related robotics and information technologies," Automation in construction, 13(1), pp. 5-19

[8] Yardimci, M. A., Hattori, T., Guceri, S. I., and Danforth, S., 1997, "Thermal analysis of fused deposition," Proceedings of solid freeform fabrication conference, pp. 689-698

[9] Atif Yardimci, M., and Güçeri, S., 1996, "Conceptual framework for the thermal process modelling of fused deposition," Rapid Prototyping Journal, 2(2), pp. 26-31

[10] Rodríguez, J. F., Thomas, J. P., and Renaud, J. E., 2001, "Mechanical behavior of acrylonitrile butadiene styrene (ABS) fused deposition materials. Experimental investigation," Rapid Prototyping Journal, 7(3), pp. 148-158

[11] Zhang, Y., and Chou, Y., 2006, "Three-dimensional finite element analysis simulations of the fused deposition modelling process," Proceedings of the Institution of Mechanical Engineers, Part B: Journal of Engineering Manufacture, 220(10), pp. 1663-1671

[12] Zhang, Y., and Chou, K., 2008, "A parametric study of part distortions in fused deposition modelling using three-dimensional finite element analysis," Proceedings of the Institution of Mechanical Engineers, Part B: Journal of Engineering Manufacture, 222(8), pp. 959-968

[13] Li, L., 2002, Analysis and fabrication of FDM prototypes with locally controlled properties, University of Calgary.

[14] Rodriguez, M. J., 2000, "Modeling the mechanical behavior of fused deposition acrylonitrile-butadiene-styrene polymer components,"

[15] Costa, S., Duarte, F., and Covas, J., 2015, "Thermal conditions affecting heat transfer in FDM/FFE: a contribution towards the numerical modelling of the process: This paper investigates convection, conduction and radiation phenomena in the filament deposition process," Virtual and Physical Prototyping, 10(1), pp. 35-46

[16] Bukkapatnam, S., and Clark, B., 2007, "Dynamic modeling and monitoring of contour crafting-: An extrusion-based layered manufacturing process," Transactions of the ASME, Journal of manufacturing science and engineering, 129(1), pp. 135-142

[17] Fang, T., Bakhadyrov, I., Jafari, M. A., and Alpan, G., 1998, "Online detection of defects in layered manufacturing," IEEE International Conference on Robotics and Automation, pp. 254-259

[18] Peyre, P., Aubry, P., Fabbro, R., Neveu, R., and Longuet, A., 2008, "Analytical and numerical modelling of the direct metal deposition laser process," Journal of Physics D: Applied Physics, 41(2), p. 025403

[19] He, K., Wang, H., and Hu, H., 2018, "Approach to Online Defect Monitoring in Fused Deposition Modeling Based on the Variation of the Temperature Field," Complexity, 2018

[20] Wu, H., Yu, Z., and Wang, Y., 2017, "Real-time FDM machine condition monitoring and diagnosis based on acoustic emission and hidden semi-Markov model," The International Journal of Advanced Manufacturing Technology, 90(5-8), pp. 2027-2036

[21] Dinwiddie, R. B., Love, L. J., and Rowe, J. C., 2013, "Real-time process monitoring and temperature mapping of a 3D polymer printing process," Thermosense: Thermal Infrared Applications XXXV, p. 87050L

[22] Kousiatza, C., and Karalekas, D., 2016, "In-situ monitoring of strain and temperature distributions during fused deposition modeling process," Materials & Design, 97, pp. 400-406

[23] Bastien, L., and Gillespie Jr, J., 1991, "A non-isothermal healing model for strength and toughness of fusion bonded joints of amorphous thermoplastics," Polymer Engineering & Science, 31(24), pp. 1720-1730

[24] Bathe, K.-J., 2006, Finite element procedures, Klaus-Jurgen Bathe.

[25] Hughes, T. J., 2012, The finite element method: linear static and dynamic finite element analysis, Courier Corporation.

[26] Reddy, J. N., and Gartling, D. K., 2010, The finite element method in heat transfer and fluid dynamics, CRC press.

[27] Strang, G., and Fix, G. J., 1973, An analysis of the finite element method, Prentice-hall Englewood Cliffs, NJ.

[28] Rao, P. K., Liu, J., Roberson, D., Kong, Z., and Williams, C., 2015, "Online Real-Time Quality Monitoring in Additive Manufacturing Processes Using Heterogeneous Sensors," Journal of Manufacturing Science and Engineering, 137(6), pp. 061007-061007-061012.doi:10.1115/1.4029823

[29] Huang, Y., Leu, M. C., Mazumder, J., and Donmez, A., 2015, "Additive Manufacturing: Current State, Future Potential, Gaps and Needs, and Recommendations," Journal of Manufacturing Science and Engineering, 137(1), pp. 014001-014001-014010.doi:10.1115/1.4028725